Biophysical Journal Volume 86 March 2004 1777–1793

Quantitative Analysis of the Viscoelastic Properties of Thin Regions of Fibroblasts Using Atomic Force Microscopy

R. E. Mahaffy,* S. Park,* E. Gerde,*† J. Käs,‡ and C. K. Shih*¶‖

*Department of Physics, †Center for Nonlinear Dynamics, University of Texas, Austin, Texas; ‡Fakultät für Physik und Geowissenschaften, Universität Leipzig, Leipzig, Germany; and ¶Texas Materials Institute, ‖Center for Nano and Molecular Science, University of Texas, Austin, Texas

ABSTRACT Viscoelasticity of the leading edge, i.e., the lamellipodium, of a cell is the key property for a deeper understanding of the active extension of a cell's leading edge. The fact that the lamellipodium of a cell is very thin (<1000 nm) imparts special challenges for accurate measurements of its viscoelastic behavior. It requires addressing strong substrate effects and comparatively high stresses (>1 kPa) on thin samples. We present the method for an atomic force microscopy-based microrheology that allows us to fully quantify the viscoelastic constants (elastic storage modulus, viscous loss modulus, and the Poisson ratio) of thin areas of a cell (<1000 nm) as well as those of thick areas. We account for substrate effects by applying two different models—a model for well-adhered regions (Chen model) and a model for nonadhered regions (Tu model). This method also provides detailed information about the adhered regions of a cell. The very thin regions relatively near the edge of NIH 3T3 fibroblasts can be identified by the Chen model as strongly adherent with an elastic strength of ~1.6 ± 0.2 kPa and with an experimentally determined Poisson ratio of ~0.4 to 0.5. Further from the edge of these cells, the adherence decreases, and the Tu model is effective in evaluating its elastic strength (~0.6 ± 0.1 kPa). Thus, our AFM-based microrheology allows us to correlate two key parameters of cell motility by relating elastic strength and the Poisson ratio to the adhesive state of a cell. This frequency-dependent measurement allows for the decomposition of the elastic modulus into loss and storage modulus. Applying this decomposition and Tu's and Chen's finite depth models allow us to obtain viscoelastic signatures in a frequency range from 50 to 300 Hz, showing a rubber plateau-like behavior.

INTRODUCTION

Eukaryotic cells reversibly assemble protein filaments (actin filaments, intermediate filaments, and microtubules) and accessory proteins into extensive three-dimensional networks. The dynamic nature of these networks allows the cell to move by extending and remodeling peripheral elastic lamellipodia in the direction of locomotion (Stossel, 1993). These lamellipodia are large, broad protrusive regions that are found at leading edges of advancing cells. The actin cytoskeleton addresses the lamellipodial protrusion through actin polymerization in conjunction with other accessory proteins (Borisy and Svitkina, 2000; Pantaloni et al., 2001). Since viscoelastic changes, i.e., gel-sol transitions, are the basic elements of cell motility, spatially resolved measurements of the cell's viscoelastic behavior are quintessential to the understanding of the cytoskeletal machinery that advances the cell. However, atomic force microscopy (AFM)-based measurements of this property are complicated by the fact that the lamellipodium is very thin (~100–1000-nm thick), resulting in a strong substrate effect. In addition, for biological cells, the issue is complicated by the strongly nonlinear response of cells to deformations, making them able to withstand stresses of >10 kPa and yet deform readily to slight pressures when adhering to neighboring cells. Thus, a technique for this application must provide the ability to probe a wide range of stresses and start at relatively low stresses where the cell responds linearly.

Previous studies have attempted to obtain information on the viscoelastic properties both locally, at measurement points within a cell, and globally, throughout the entire cell. Several tools measure whole-cell elasticity in suspension such as micropipette aspiration (Evans and Yeung, 1989; Discher et al., 1994; Tsai et al., 1994; Lelièvre et al., 1995), optical tweezers (Hénon et al., 1999), and the optical stretcher (Guck et al., 2000). In addition, attached fibroblast cells have been globally characterized through microplate manipulation (Thoumine and Ott, 1997), the elastic substrate method (Dembo and Wang, 1999), and the monitoring of fluorescent bead markers in a cell under deformation by an adjacent cell (Ragsdale et al., 1997). An average global elasticity was characterized using a conventional rheometer on cell pellets (Eichinger et al., 1996). These characterizations of global mechanical properties contribute vital information on the differences in mechanical strength of different cell lines. However, they cannot illuminate the mechanisms of changes in local viscoelastic properties of motile cells.

Local measurements of a cell's viscoelastic properties within micron or submicron regions can reveal information on cell motion and local structural changes in response to alterations in cell function (Elson, 1988; Rotsch et al., 2001). Cell poking represents the first attempt to characterize local elastic properties accurately (Petersen et al., 1982). Local viscoelastic information is available through bead

Submitted May 21, 2002, and accepted for publication October 27, 2003.

S. Park and R. E. Mahaffy contributed equally to this work.

Address reprint requests to C. K. Shih, E-mail: shih@physics.utexas.edu.

R. E. Mahaffy's present address is KBT 542 MCDB Yale University, PO Box 208103, New Haven, CT 06520-8103.

0006-3495/04/03/1777/17 $2.00

microrheology using embedded or attached magnetic beads (Ziemann et al., 1994). Microrheology with beads based on laser-interferometry provides high frequency and low stress information (Amblard et al., 1996). Similar methods have been applied using naturally occurring particles in kidney epithelial cells (Yamada et al., 2000). Even though these techniques are the most effective in the low stress regime (<500 Pa), the measurement points are limited to the placed bead or the naturally occurring particle in the cell.

AFM providing the method for nanoindentations has advantages, such as adaptability to the liquid environment, the ability to measure forces precisely in a localized region, and repeatability. Although versatile, the AFM technique has been challenged with the effects of the underlying substrate in the thin regions of the cell.

Comparative AFM studies measured relative elastic moduli between different areas within a cell or between different types of cells (A-Hassan et al., 1998; Goldmann et al., 1998; Lekka et al., 1999). Some progress has been achieved by modeling the commercial AFM tip as a conical indenter to obtain absolute elasticity values of different cell lines (Rotsch et al., 1999; Radmacher et al., 1996). However, measurable contributions from the underlying hard substrate are quickly observed under the high stresses (>1 kPa) produced by these sharp tips (Domke and Radmacher, 1998).

Finally, in many previous AFM experiments, the cell's viscous properties have been only qualitatively observed from phase differences between an oscillating sample and the responding tip (Radmacher et al., 1992, 1996). Recent alterations to the standard Hertz model and a modified AFM tip have allowed for the determination of the quantitative viscoelastic properties of thick regions of the cell with a controlled nondestructive stress range (100 Pa to 10 kPa) (Mahaffy et al., 2000).

Besides the applied force and the contact area of the probe, the thickness of the sample also determines the stress on the sample. The determination of the viscoelastic constants relies on an accurate model reflecting the geometry of the system. By attaching a polystyrene bead at the end of the AFM tip, we obtain a well-defined spherical probe that allows us to model the mechanical behavior accurately by adopting the Hertz model (Landau and Lifshitz, 1959). In addition, because the size of the beads is of the order of μm, a larger contact area allows us to reduce the stress on the sample.

Nevertheless, thin samples require more sophisticated models. To overcome substrate effects and high strains, we applied two additional models for thin regions. Similar models have been applied to polymer films to obtain elastic moduli (Dimitriadis et al., 2002). However, with respect to Dimitriadis et al., our results show a fundamentally different dependency on the Poisson ratio that is consistent with the original work of Tu and Chen.

The regions where the cytoskeleton adheres to the substrate and where it does not, require slightly different modeling approaches. For areas such as the leading edge where the cytoskeleton adheres the substrate, our modeling approach is based on the early work of Chen and co-worker. Thus, we call this approach the Chen model (Chen, 1971; Chen and Engel, 1972). The Chen model has a significant advantage inasmuch as it determines both the elastic constant and the Poisson ratio. In all previous measurements of viscoelastic properties of the cell, the Poisson ratio was not experimentally accessible, and was assumed for the deduction of the elastic modulus. Regions further from the edge are poorly attached to the substrate and thus require another model that we will call the Tu model since it is based on Tu's early work (Tu and Gazis, 1964). The Tu model as well as the Chen model can be extended to deal with frequency-dependent viscoelastic contributions and therefore allow us to accurately investigate the viscoelastic behavior in the thin regions of cells that were previously quantitatively inaccessible with the AFM.

THEORY

Our discussion of the theoretical models begins with the Hertz model and the viscoelastic extension of the Hertz model since it contains the basic ideas of all AFM-based microrheological measurements. Then we explore how to extend the Hertz model in the very thin regions by introducing the finite boundary conditions of the Chen and the Tu models.

The Hertz model and its viscoelastic extension

The Hertz model provides a good example of how an elastic model can be extended to include viscoelastic contributions and can be used for the thick areas of a cell (Mahaffy et al., 2000). This model relates the quantities of the deforming force, f_{bead}, to the indentation, δ. Included are the radius of the probe, R, and the elastic constant, $K = E/(1-\nu^2)$, which depends on the Young's modulus, E, and the Poisson ratio, ν,

$$f_{\text{bead}} = \frac{4}{3} K R^{1/2} \delta^{3/2}. \quad (1)$$

Two important assumptions are made in deriving Eq. 1. First, the indenter is assumed to have a paraboloid shape. Previous measurements have shown that this assumption remains valid in the case that a spherical tip is much larger than the indentations ($\delta < 0.3\,R$; Mahaffy et al., 2000). Second, the indented sample is assumed to be extremely thick in comparison to the indentation ($h >> \delta$, h is the sample thickness). The latter assumption is inaccurate for the thin lamellipodial regions of cells, but is effective in regions away from the cell boundary for small indentations.

The Hertz model was designed for soft materials showing only an elastic behavior. However, a single elastic Young's modulus is insufficient to characterize the behavior of a complex polymer system such as a cell's cytoskeleton. The cytoskeleton can show a strong viscous response as well as an elastic response to deformation and respond actively on longer timescales. For this reason, dynamic measurements

must be performed to measure the frequency-dependent viscoelastic behavior.

Dynamic measurements are done by introducing a high frequency (>20 Hz), but low amplitude (5–10 nm) oscillation to the system. An oscillation introduced in the sample height (drive oscillation) results in an oscillation of the cantilever resting on the sample surface with amplitude and phase differences that depend on the viscoelastic properties of the intervening sample. In this case, the oscillating indentation, $\tilde{\delta}^*$, is superimposed on an offset indentation, δ_0. Thus, the total indentation, δ, is

$$\delta = \delta_0 + \tilde{\delta}^* e^{i\omega t} \tag{2}$$

with

$$\tilde{\delta}^* = \delta' + i\delta''.$$

For viscoelastic materials, such as cells, the Hertz model must be extended to include frequency-dependent behavior. The extended model can be obtained by expanding the Hertz model in the indentation, δ, by a Taylor series, as

$$f_{\text{bead}} \approx \frac{4}{3}R^{1/2}\left(K_0\delta_0^{3/2} + 3/2\ K_1^*\delta_0^{1/2}\ \tilde{\delta}^*\right), \tag{3}$$

with

$$K_i = \frac{E_i}{1-\nu^2}, (i = 0, 1, \ldots).$$

The constant, K_1^*, is complex as indicated by the asterisk. This two-term expansion is valid when the amplitude of the oscillating indentation is much smaller than the offset indentation, δ_0. Here, f_{bead} can be decomposed into two terms, as

$$\begin{aligned} f_0 &\equiv \frac{4}{3}K_0R^{1/2}\delta_0^{3/2} \\ f_{\text{osc}}^* &\equiv 2K_1^*R^{1/2}\delta_0^{1/2}\ \tilde{\delta}^*. \end{aligned} \tag{4}$$

The first term, f_0, is simply the contribution of the original Hertz model. The second term, f_{osc}^*, is related to the viscoelastic constant, K_1^*, which is determined by the following function of measurable values:

$$K_1^* = \frac{f_{\text{osc}}^*}{2\tilde{\delta}^*(R\delta_0)^{1/2}} = K' + iK''. \tag{5}$$

Both f_{osc}^* and $\tilde{\delta}^*$ contain real and imaginary parts corresponding to the components of the measured signal that are in-phase and 90° out-of-phase with the driving signal, respectively. The real part, K', reflects the elastic storage response, whereas the imaginary part, K'', reflects the viscous loss response of the sample.

As with the original Hertz model, deviations in the viscoelastic constant as a function of δ_0 can occur due to the finite sample depth, a static nonuniformity in the cell structure with depth, or dynamic changes in the viscoelastic modulus during a measurement. The latter of these effects represents phenomena that could provide strong insights into the dynamics of the cytoskeleton. A key issue toward investigating viscoelastic properties is the elimination of the effect of the finite sample depth. We address this issue with two additional models described in the following sections.

Nonadhered thin regions of cells—the Tu model

There are two asymptotic regimes for modeling the deformation of a layer on a substrate. These regimes are a rigidly adhered layer, which is unable to move at the sample substrate interface, and a nonadhered layer, which slides freely on the substrate. By applying the proper boundary conditions, we can solve the two different regimes using the method, originally developed for the rigidly adhered condition. We begin with the simpler nonadhered condition.

The problem of a spherical body impacting a nonadhered layer on a substrate was first addressed and mathematically described by Popov (1962). Tu and co-worker numerically solved this problem for a limited range of thickness (Tu and Gazis, 1964). The complete solution can be found by using methods developed by Chen and co-worker (Chen, 1971; Chen and Engel, 1972). The model by Chen was originally used for the rigidly adhered case, but it can be adopted for the nonadhered case under the proper boundary conditions without limits on the sample thickness.

The approach by Chen applies to media composed of several layers each with a different elastic modulus. In our case, the Chen model can be reduced to a single elastic layer on a hard incompressible substrate. In Chen's article, the contact problem is solved as a boundary value problem and the solutions are assumed to be a series expansion of the standard Hertz model solution. Thus, the total pressure distribution on the sample is the sum over a series of partial pressure distributions (see Appendix Eq. A1). The series expansion inherently means that the Tu and the Chen models approach the Hertz solution for small indentations or for thick samples.

In the nonadhered case, the boundary conditions are analogous to those of two identical spheres indenting a layer of twice the actual thickness, $2h$ (see Fig. 1). (In Chen's article, they consider a layer of a double thickness, $2h$ on a hard substrate, and this is very useful in this problem.) In essence, it is a mirror-image problem with all the appropriate boundary conditions.

With the earlier definition of $K = E/(1-\nu^2)$, we find the following relation between the elastic constants predicted by the Hertz and the Tu model (for the detailed derivations, see the Appendix):

$$\frac{K_{\text{Hertz}}}{K_{\text{Tu}}} = \frac{3\pi}{4}\frac{a_{\text{Tu}}}{a_{\text{Hertz}}}\sum_{i=1}^{N}\frac{p_i^T}{1+2i} \tag{6}$$

with

$$a_{\text{Tu}} \equiv a, \quad a_{\text{Hertz}} \equiv (R\delta)^{1/2}.$$

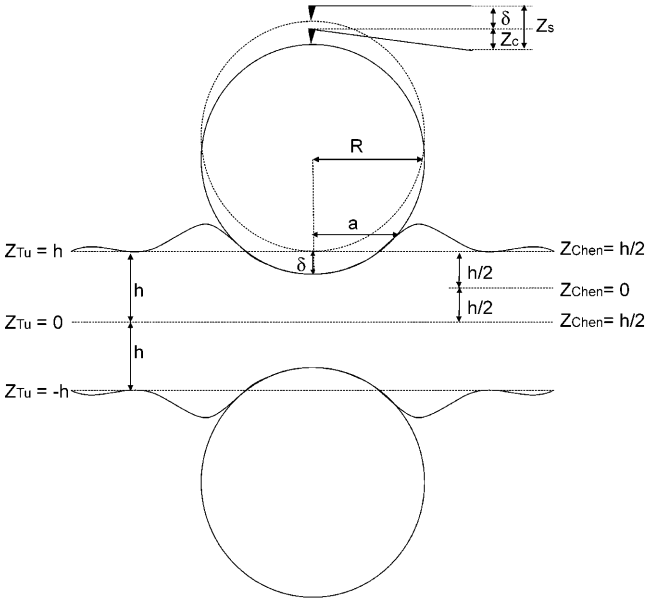

FIGURE 1 A schematic diagram representing a spherical AFM probe impacting an elastic layer on a hard substrate. The indentation, δ, was calculated by subtracting the cantilever deflection, z_c, from the scanner displacement, z_s. The coordinates relevant to the Chen and the Tu models are z_{Chen} and z_{Tu}, respectively. In the Tu model, lateral displacements are unconstrained and there is no lateral stress within the contact areas between the sample and the hard substrate. The boundary conditions for this problem are the same as those of two equal spheres colliding with a layer of twice the thickness of the real sample, $2h$. The boundary conditions of the Chen model include the fact that the sample is rigidly bound to a substrate without lateral motion at the interface. A sphere colliding with a layer of the thickness, h, supported on the hard adherent substrate is sufficient to describe this boundary condition.

Here a is the contact radius and the subscript indicates the applicable model. The superscript of p_i^T indicates that these values are specific to the Tu model. They differ from the p_i originally defined in Eq. A1 and the p_i^c defined later for the Chen model in that $(1-\nu)$ is factored out, i.e., $p_i^T = p_i/(1-\nu)$. Consequently, K_{Tu} displays the same dependence on the Poisson ratio as the Hertz model and the ratio of K_{Hertz}/K_{Tu} is independent of the Poisson ratio. This also implies that p_i^T is independent of the Poisson ratio. The values of p_i^T were numerically calculated and used to find the ratio of the K values predicted by the Hertz and Tu models, i.e., K_{Hertz}/K_{Tu}, for various indentations. The required order N in the series expansion was determined by comparing successive values of N and looking for a change of $<0.1\%$ in the ratio of K_{Hertz}/K_{Tu} over the entire range of indentations. A value of $N = 4$ is sufficient to meet this requirement even for extremely thin samples.

Adhered thin regions of cells—the Chen model

Several groups have investigated the problem of a spherical probe indenting a rigidly adhered film of arbitrary thickness (Biot, 1935; Burmister, 1945; El-Sherbiney and Halling, 1976; Ogilvy, 1993; Vorovich and Ustinov, 1959). Chen and co-worker presented one solution that applies for a large range of indentations in two successive articles (Chen, 1971; Chen and Engel, 1972). Unlike the Tu model, the boundary conditions are not symmetric (see Fig. 1). The detailed derivations of K_{Chen} can be found in the Appendix.

For the Chen model, indicated by the superscript, the values p_i^c are dependent on the Poisson ratio in a way that cannot be factored out. Thus, for the Chen model, the ratio of K_{Hertz}/K_{Chen} is dependent on the Poisson ratio, as

$$\frac{K_{Hertz}}{K_{Chen}} = \frac{3\pi}{4}(1-\nu)\frac{a_{Chen}}{a_{Hertz}}\sum_{i=1}^{N}\frac{p_i^c(\nu)}{1+2i}, \tag{7}$$

with

$$a_{Chen} \equiv a, \quad a_{Hertz} \equiv (R\delta)^{1/2}.$$

Like the Tu model, the p_i^c values are calculated numerically. The expressions in Eq. 7 are used to convert the values calculated by the Hertz model to those by the Chen model.

Viscoelastic extension of the Tu and the Chen models

The viscoelastic extension of the Tu and the Chen models follows the previous extension of the Hertz model. In both models, an independent variable, $\delta R/h^2$, containing all experimentally relevant quantities can be extracted and assigned to a single variable, x ($\equiv \delta R/h^2$). The general form of the applied force, f_{bead}, is

$$f_{bead} = Kf(x). \tag{8}$$

In analogy to the extended Hertz model, this force can be expanded in a Taylor series in terms of the indentation, as

$$f_{bead} = K_0 f(x) + K_1^* \frac{df}{dx}\frac{dx}{d\delta}. \tag{9}$$

The $dx/d\delta$ can be calculated explicitly as

$$f_{bead} = K_0 f(x) + K_1^* \frac{R}{h^2}\frac{df}{dx}\delta^*. \tag{10}$$

The oscillatory force, f_{osc}^*, is given by the second term of Eq. 10, which is

$$f_{osc}^* = K_1^* \frac{R}{h^2}\frac{df}{dx}\delta^*. \tag{11}$$

By comparing the oscillatory force, f_{osc}^*, in Eq. 11 with that from the Hertz model in Eq. 4, the relative viscoelastic value, $K_{Tu1,Chen1}^*/K_{Hertz1}^*$, is calculated as follows:

$$\frac{K_{Tu\,1,Chen\,1}^*}{K_{Hertz\,1}^*} = \frac{2h^2\delta_0^{1/2}}{R^{1/2}\left(\frac{df}{dx}\right)}. \tag{12}$$

Each subscript indicates the model used. Following from Eq. A14 and Eq. 12, the ratio of viscoelastic constants,

$K^*_{\mathrm{Tu1,Chen1}}/K^*_{\mathrm{Hertz1}}$, can be obtained from the following equation for the new models:

$$\frac{K^*_{\mathrm{Tu\ 1,Chen\ 1}}}{K^*_{\mathrm{Hertz\ 1}}} = \frac{2^{1/2}}{\pi\left(3/2\ S_{\mathrm{Tu,Chen}}\beta^{1/2} + x\partial(S_{\mathrm{Tu,Chen}}\beta^{1/2})/\partial x\right)}, \tag{13}$$

with

$$\beta = \frac{a^2}{2R\delta},\ S_{\mathrm{Tu}} = \sum_{\mathrm{i}=1}^{\mathrm{N}} p_{\mathrm{i}}^{\mathrm{T}}/(1+2i),\ S_{\mathrm{Chen}} = (1-\nu)\sum_{\mathrm{i}=1}^{\mathrm{N}} p_{\mathrm{i}}^{\mathrm{c}}/(1+2i).$$

The values of β, S, and the derivative function, $\partial(\mathrm{S}\beta^{1/2})/\partial x$, were calculated numerically for a full range of indentations. With this information and the complex modulus obtained using the Hertz model, K^*_{Hertz1}, the viscoelastic properties can be evaluated even for thin cell regions.

MATERIALS AND METHODS

Cells

The data were taken from NIH 3T3 fibroblasts and H-ras-transformed fibroblasts (American Type Culture Collection, Manassas, VA). The NIH 3T3 fibroblasts were cultured with Dulbecco's modified Eagle's medium, DMEM (American Type Culture Collection), supplemented with 10% calf serum (American Type Culture Collection). For *H-ras*-transformed fibroblasts, fetal bovine serum (American Type Culture Collection) was substituted for calf serum. To keep the pH constant (~7.4) during AFM measurements, we added 10 mM HEPES (Sigma Aldrich, St. Louis, MO) to the medium. For the experiments, cells were plated on the presterilized coverslips a day before data were taken. We incubated them at 37°C in 5% CO_2 atmosphere. For AFM measurements, we continuously provided small amounts of the medium solution to the cells through the inlet of the liquid cell (Microcell, TM Microscopes, Sunnyvale, CA). To ensure the viability of the investigated cells we stopped the measurements ~2 h after removing the cells from the incubator.

Optical microscopy

For fluorescence microscopy, cells were fixed for 10 min with 3.7% formaldehyde. After being washed with phosphate-buffered saline (PBS), the cells were permeabilized with 0.1% Triton in PBS. To visualize the actin filaments, cells were stained with 0.1% TRITC-phalloidin in PBS (Sigma Aldrich) in PBS for 10 min at room temperature, subsequently washed with PBS, and mounted on the cover slide. Fluorescence images were taken with a confocal microscope (LSM 510, Carl Zeiss, Jena, Germany). Reflection interference contrast images of cells adhered to a glass coverslip were taken using a reflection interference contrast objective (63×, $NA = 1.25$, Carl Zeiss).

AFM—tip modification

As mentioned in the Introduction, to avoid damaging the sample and any nonlinear deforming stress, the AFM tip geometry was modified to a well-defined sphere. The cantilevers used in the experiments were commercial Microlevers (TM Microscopes) with force constants between 0.02 and 0.06 N/m. The spherical probes were constructed by gluing polystyrene beads (Seradyn Particle Technology, Indianapolis, IN), ranging in radii from 1.5 to 4 μm to the AFM tips using standard TEM epoxy with a low viscosity, M-Bond 610 (SPI Supplies, West Chester, PA). After curing them overnight at 85°C, the probes were characterized thoroughly by reverse imaging over a sharp AFM tip to assure that the bead on the tip was well-centered (see *inset* in Fig. 2). The AFM topographic images provided the exact radius and the overall state of the bead (see Fig. 2). Once the probe geometry had been accurately characterized, the force constant of each cantilever was calibrated. The most accurate values were obtained when calibrating against a cantilever with a similar force constant. For this purpose, we prepared standard cantilevers with a comparable force constant, k, using three approaches to crosscheck the accuracy. Our standard cantilevers were calibrated using a commercial cantilever (TM Microscopes) of known force constant, 0.157 N/m (Tortonese and Kirk, 1997) and by analyzing their thermal fluctuations (Butt and Jaschke, 1995). Furthermore, the resonance frequency and cantilever dimensions were measured (Tortonese and Kirk, 1997) to independently determine the force constant. We selected the standard cantilevers from those that agreed within 5% in their force constants determined by the three different methods. These standard cantilevers served as calibration cantilevers with known force constants (k_{known}) to characterize unknown cantilevers with attached beads. The calibration of cantilevers with beads was done by measuring its deflection on a hard substrate ($z_{\mathrm{c(hard)}}$) as well as on our standard cantilever ($z_{\mathrm{c(can)}}$). To avoid relative errors due to scanner hysteresis or drift, the cantilever deflection was measured using the scanner detector signal. The unknown force constant (k_{unknown}) is given by the formula

$$k_{\mathrm{unknown}} = k_{\mathrm{known}}\left[\frac{z_{\mathrm{c(hard)}} - z_{\mathrm{c(can)}}}{z_{\mathrm{c(can)}}}\right]. \tag{14}$$

AFM—oscillatory measurements

All viscoelastic measurements were taken with an Autoprobe CP atomic force microscope (Park Scientific Instruments, Sunnyvale, CA). A slow indentation on the surface and subsequent retraction provided the force curve for the elastic response. The resulting approach curve was used for the calculations of the zero-frequency elastic modulus.

The experimental setup to perform the viscoelastic measurements is illustrated in Fig. 3. The main component of the frequency-dependent viscoelastic measurement was a small amplitude (2–5 nm), high frequency (50–300 Hz) oscillatory drive signal superposed with the slowly changing force curve signal. The higher frequency signal was added to the scanner signal through a custom-made amplifier from a dual-channel lock-in amplifier, SR830 (Stanford Research Systems, Sunnyvale, CA). The time constant of the lock-in amplifier was 1 × 100 ms at frequencies <300 Hz.

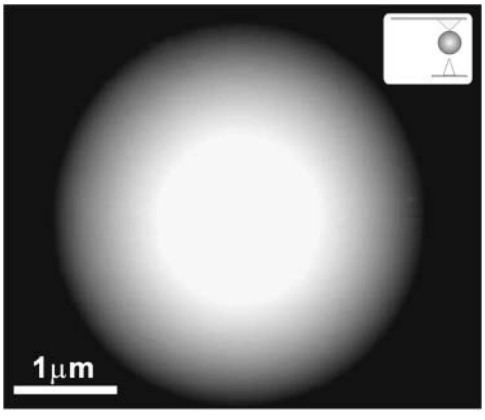

FIGURE 2 An AFM topographic image of a spherical probe used in our experiments. The inset illustrates the reverse imaging approach that uses a sharp AFM tip placed on the substrate to image the modified tip.

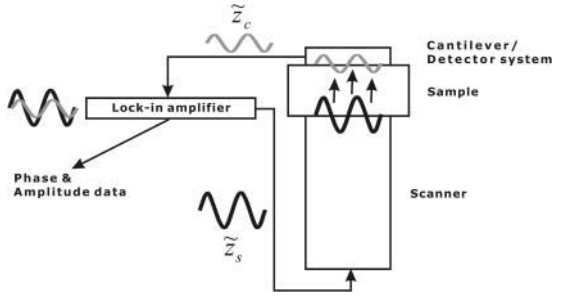

FIGURE 3 The experimental setup used to obtain the viscoelastic data. Modifications were made to a commercial AFM system to obtain the frequency-dependent viscoelastic data. The scanner was modulated by a small amplitude (5–20 nm), sinusoidal signal, $\tilde{z}_s$. A lock-in amplifier was used to detect the amplitude and the phase of the cantilever response, $\tilde{z}_c$.

This oscillatory drive signal had a small amplitude and was significantly faster than the speed of the approach curve. The detected signal from the cantilever was retrieved through a breakout box and sent to a lock-in amplifier. The time to obtain a complete force curve depended on the frequency of the oscillatory signal. As an example, it took 50 s to complete the force curve at 50 Hz and 30 s at 150 Hz.

The amplitude of the scanner drive signal, a_{drive}, was calibrated by pressing against a glass slide where the response and drive signals were in-phase and of approximately equal amplitudes. The amplitude of the response signal from the cantilever, a_{response}, was measured by the dual photodiode detectors of the AFM. The frequency, ω, of the drive signal was determined by the output of the lock-in amplifier.

The phase and amplitude data were fed back to the computer through two unused channels of the AFM data acquisition board. Thus, the data from the lock-in amplifier were included in the data stream from the scanner position sensors and total cantilever deflection sensors, which were used to determine the total indentation, δ, the oscillating indentation, $\tilde{\delta}^*$, and the total force, f_{total}.

DATA ANALYSIS

Indentations

For a measurement of the static elastic Young's modulus, the indentation, δ, was calculated from the scanner displacement, z^{s}, minus the cantilever deflection, z^{c} (see Fig. 1), $\delta = z^{\text{s}} - z^{\text{c}}$. Here, z^{c} has already been corrected for the contact point. The force, f_{bead}, was calculated from the cantilever displacement, z^{c}, and the force constant of the cantilever, k,

$$f_{\text{bead}} = kz^{\text{c}}. \tag{15}$$

For the frequency-dependent modulus, the drive oscillation was added to the offset displacement. The exact position of the sample and tip was the sum of the offset displacement and the added oscillation (see Fig. 3), as

$$\begin{aligned} z_{\text{s}} &= z_0^{\text{s}} + \tilde{z}_{\text{s}} e^{i\omega t} \\ z_{\text{c}} &= z_0^{\text{c}} + \tilde{z}_{\text{c}}^* e^{i\omega t}, \end{aligned} \tag{16}$$

where $z_0{}^{\text{s}}$ is the offset displacement of the scanner, and $z_0{}^{\text{c}}$ is the offset displacement of the cantilever after the contact is made between the tip and the sample. In a sample with viscous properties, the oscillatory cantilever deflection, $\tilde{z}_{\text{c}}^*$, includes a phase factor, φ, that differs from the oscillatory scanner deflection, $\tilde{z}_{\text{s}}$, as

$$\begin{aligned} \tilde{z}_{\text{s}} e^{i\omega t} &= a_{\text{drive}} e^{i\omega t} \\ \tilde{z}_{\text{c}}^* e^{i\omega t} &= a_{\text{response}} (\cos\varphi - i \sin\varphi) e^{i\omega t}. \end{aligned} \tag{17}$$

The variable a_{drive} is the amplitude of the oscillatory scanner deflection, a_{response} is the amplitude of the oscillatory cantilever deflection, and ω is the driving frequency.

The offset indentation, δ_0, was determined by subtracting the cantilever motion from the scanner displacement, $\delta_0 = z_0{}^{\text{s}} - z_0{}^{\text{c}}$. The cantilever and the scanner displacements were determined by subtracting the contact point as discussed below. The oscillating indentation, $\tilde{\delta}*$, was found by subtracting $\tilde{z}_{\text{c}}^*$ from $\tilde{z}_{\text{s}}$. An example of the raw data of $\tilde{z}_{\text{c}}^*$ is shown in Fig. 4 *B*. In-phase and out-of-phase parts of the oscillatory cantilever signal were plotted as a function of the offset displacement of the scanner, z_0^{s}.

Hydrodynamic drag force

In the oscillatory viscoelastic measurements, the viscous medium surrounding the entire cantilever resulted in a drag force that was solely due to the effects of the surrounding medium and was unrelated to viscous effects of the sample. The oscillating drive on the sample caused a drag force on the cantilever, f_{drag}^*, which could be approximated by (Mahaffy et al., 2000)

$$f_{\text{drag}}^* = i\omega\gamma\tilde{\delta}^*. \tag{18}$$

The constant γ contains the viscosity of the medium and the effective size of the cantilever. The constant γ was determined by monitoring the cantilever oscillation, $\tilde{z}_{\text{c}}^{*0}$, in response to the scanner oscillation, $\tilde{z}_{\text{s}}^0$, before making contact with the sample (here the superscript, ^{0}, denotes that it was before contact). This measurement was performed directly before the tip made contact, i.e., as close as possible to the surface considering that hydrodynamic friction, i.e., drag, increased close to a surface. The further increase in friction after contact stemmed from the viscoelastic properties of the cell. Close to contact, the drag force was measured directly by monitoring the cantilever oscillation, i.e., $f_{\text{drag}}^* = i\omega\gamma(\tilde{z}_{\text{s}}^0 - \tilde{z}_{\text{c}}^{*0}) = k\tilde{z}_{\text{c}}^{*0}$. The expression for the constant, γ, can be simplified because the cantilever oscillation close to contact was relatively small in comparison to the drive signal ($|\tilde{z}_{\text{s}}^0| \gg |\tilde{z}_{\text{c}}^{*0}|$),

$$\gamma = -\frac{ik}{\omega}\left(\frac{\tilde{z}_{\text{c}}^{*0}}{\tilde{z}_{\text{s}}^0 - \tilde{z}_{\text{c}}^{*0}}\right) \approx -\frac{ik}{\omega}\frac{\tilde{z}_{\text{c}}^{*0}}{\tilde{z}_{\text{s}}^0}. \tag{19}$$

Using the expression above, γ can be calculated and then repeatedly used to determine the effect of the cantilever drag on the total force for each indentation measured while in

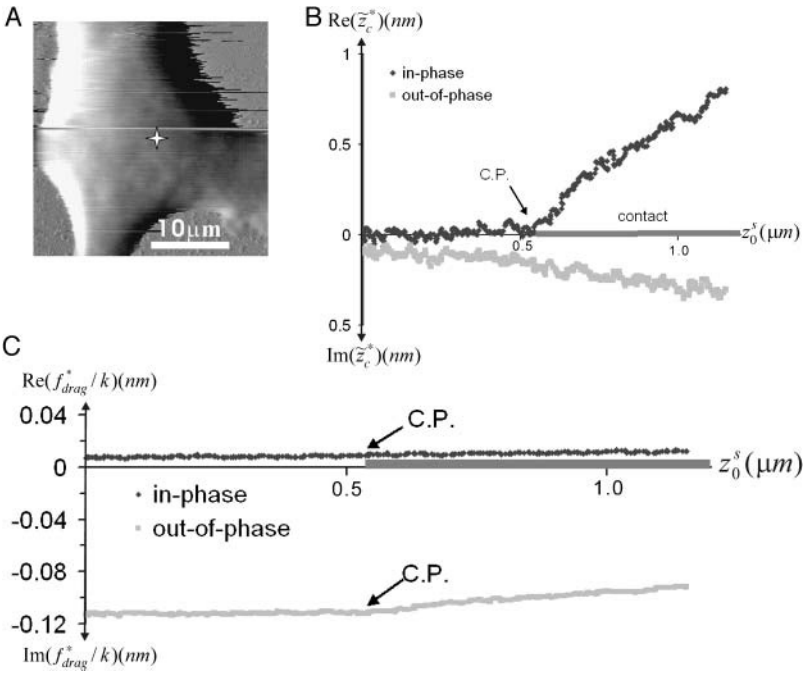

FIGURE 4 Viscoelastic data of a fibroblast cell obtained at a frequency of 50 Hz and a drive amplitude of 5 nm. The contact point of the tip with the sample, *C.P.*, is marked and the contact region is marked as the gray bar on the horizontal axis. (*A*) Error-mode image of the investigated NIH 3T3 fibroblast. The gray scale represents the height profile of the image. The point of measurement is marked by a star. (*B*) The real (in-phase) and imaginary (90° out-of-phase) oscillatory cantilever deflection, plotted as a function of the offset displacement of the scanner, z_0^s. (*C*) The cantilever drag force due to the surrounding media, plotted as a function of the offset displacement of the scanner, z_0^s. Note that the drag force is normalized to the cantilever force constant, thus having the unit of displacement. The out-of-phase viscous response is more significant than the in-phase response. The drag force is measured directly before contact. After contact, the drag force is obtained using Eq. 18.

contact with the sample. The cantilever drag does contribute significantly to the out-of-phase (viscous) component. An example is shown in Fig. 4 *C*. As expected for the motion through a fluid, the in-phase response was small and the out-of phase response was more significant. After the tip made contact with the sample, the absolute value of the out-of-phase signal dropped because less liquid moved past the cantilever and the cantilever was moving largely in-phase with the liquid. Nevertheless, the drag effect must be subtracted from the total viscoelastic force, f^*_{total}, over the range of indentation to obtain an accurate viscous constant for the sample. The total oscillatory viscoelastic force, f^*_{total}, was measured by the lock-in amplifier, as

$$f^*_{\mathrm{osc}} = f^*_{\mathrm{total}} - f^*_{\mathrm{drag}} \tag{20}$$

with

$$f^*_{\mathrm{total}} = k\tilde{z}^*_{\mathrm{c}}.$$

After the cantilever drag component had been subtracted, only the oscillatory force between the probe and the sample, f^*_{osc}, remained.

Contact point of the tip

The indentation, δ, depended on the contact point of the tip with the sample that was determined from the data. In the zero-frequency case, the contact point was simply defined as the point at which the force curve initially changed slope. The contact point was subtracted from the measured scanner displacement such that the zero point of the force curve was aligned with the contact point.

In the case of viscoelastic measurements, this point could be quickly isolated as the point at which the maximum phase change occurs. As discussed earlier, before contact, the cantilever was subject to the viscous drag of the surrounding medium leading to a constant phase difference between the cantilever response and the scanner modulation that was very close to 90°. Upon contact, the cantilever response changed immediately, causing a significant decrease in the phase shift with respect to the scanner modulation.

Sample height

The absolute height of the sample, h, is necessary in analyzing data with the Tu and the Chen models. The height was determined using a combination of the topographic image of the cell and the force curve itself. The approximate height, h_{top}, is measured directly from the topographic image of the cell. This height differs from the actual height by an amount corresponding to the imaging indentation. However, by performing the force-curve measurement, the contact point can be determined (as described above), which allows us to determine the actual height more precisely, as

$$h = h_{\mathrm{top}} + \delta_{\mathrm{top}}, \tag{21}$$

where the value δ_{top} is the slight indentation that occurs in imaging the cell.

Determination of the modulus

The constants K and K^* can be calculated from a complete force curve obtained at each frequency, including data

appearing before the contact point and extending to significant indentations. The valid indentation range for each model is determined by the range over which these calculated values, K and K^*, remain nearly constant as would be expected for linear materials. For thin lamellipodial regions, the AFM-tip indents solely the actin cortex and inhomogeneities of these actin networks occur on a length scale larger than the indenting region. For thicker regions, Ananthakrishnan and co-workers recently showed that the actin cortex dominates the elastic response (R. Ananthakrishnan J. Guck, F. Wottawah, S. Schinkinger, B. Lincoln, M. Romeyke, T. Moon, and J. Käs, unpublished). Thus, it is reasonable to assume a single viscoelastic constant over the entire range of indentations.

As an example, the plots shown in Fig. 5 demonstrate that both the real and imaginary parts of K^* from the extended Hertz model are approximately constant as a function of the indentations, δ_0, for the thick region ($h = 4.8\ \mu$m) of a fibroblast at a frequency of 50 Hz. The initial variation in K^* for small δ_0 is primarily due to uncertainties in the initial contact point. The small increases in K' are not significant compared with the increases caused by substrate effects in thin regions.

When significant increases of the viscoelastic constants were observed with increasing indentation, the data were better analyzed with the Tu or the Chen model. Our numerical calculation for these two models generated lookup tables (the numerical tables for the Tu and Chen model are available upon E-mail request to the corresponding author), in which $K^{(*)}_{\mathrm{Tu}}/K^{(*)}_{\mathrm{Hertz}}$ or $K^{(*)}_{\mathrm{Chen}}/K^{(*)}_{\mathrm{Hertz}}$ are listed as a function of $\delta R/h^2$ (see also Figs. 6 and 7). This table allows us to directly convert the complex moduli determined using the Hertz model into the proper complex moduli for the nonadhered and the well-adhered model, i.e., the Tu and the Chen models.

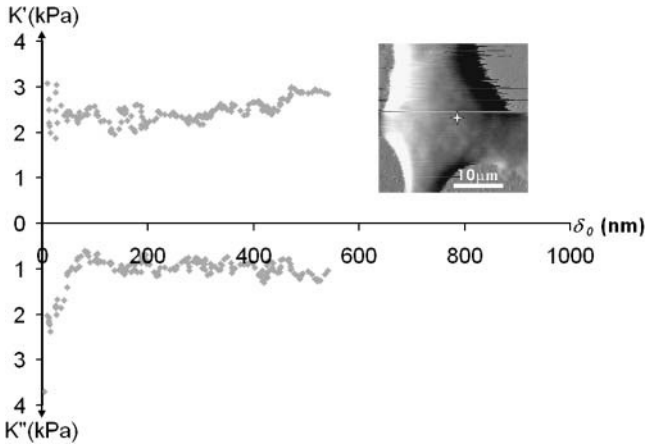

FIGURE 5 The effectiveness of the extended Hertz model for thick samples. The storage, K', and the loss modulus, K'', are plotted as a function of the indentation, δ_0. The investigated NIH 3T3 fibroblast is shown in the inset. The data were taken at the frequency of 50 Hz and the drive amplitude of 5 nm. Both the real, K', and imaginary parts, K'', remain constant over the full range of indentations, δ_0.

RESULTS AND DISCUSSION

Numerical behavior of the Tu and the Chen models

For extremely deep samples and/or shallow indentations, the Tu and the Chen solutions are equivalent to the Hertz model. This is illustrated in Figs. 6 and 7 where the ratios of the predicted contact radii, $a_{\mathrm{Tu,Chen}}/a_{\mathrm{Hertz}}$, and the predicted elastic constants, $K_{\mathrm{Tu,Chen}}/K_{\mathrm{Hertz}}$, approach 1 for large sample heights. For sample heights that are 10 times less than the Hertz contact radius, $a_{Hertz}(=\sqrt{\delta R})$, there is a significant contribution to the total force from the hard substrate, which makes the constants calculated using the Tu and the Chen models deviate from those by the Hertz model.

The ratio $K_{\mathrm{Tu}}/K_{\mathrm{Hertz}}$ is independent of the Poisson ratio. However, $K_{\mathrm{Chen}}/K_{\mathrm{Hertz}}$ does depend on the Poisson ratio (see Fig. 7). The Poisson ratio influences the degree at which the Chen model deviates from the Hertz model. A Poisson ratio of zero results in an equivalent curve to the nonadhered case treated by the Tu model. For the Chen model, a Poisson ratio of zero implies that the sample has no lateral strain coupling, which makes this case indistinguishable from the nonadhered case treated as the Tu model. However, this is an unlikely scenario for the cell cytoskeleton, and thus only Poisson ratios, ν, of 0.3 and 0.5, are shown in Fig. 7. The hard substrate is felt earlier as the Poisson ratio increases. Thus, even in relatively thick areas of the cell, the Hertz model fails where the cell is well adhered and has a high Poisson ratio. In our experiments, this deviation is rarely observed, which indicates that thick cellular areas are poorly attached to the underlying surface and/or have low Poisson ratios. The dependency of $K_{\mathrm{Chen}}/K_{\mathrm{Hertz}}$ on the Poisson ratio, ν, allows us to determine $K = E/(1-\nu^2)$ as well as the Poisson ratio. The Poisson ratio can be obtained from fitting $K_{\mathrm{Chen}}/K_{\mathrm{Hertz}}$ vs. $\delta R/h^2$ to the experimental data.

Introducing oscillations of various frequencies allows us to measure complex constants, K_1^* with real and imaginary parts, i.e., $K_1^* = K_1' + iK_1''$, which are more complete representations of the viscoelastic properties of the material. The ratios of $K_1'/K'_{\mathrm{Hertz1}}$ for the Chen model with various Poisson ratios and for the Tu model are plotted in Fig. 8. The ratio, $K_1''/K''_{\mathrm{Hertz1}}$, shows an equivalent signature as the ratio, $K_1'/K'_{\mathrm{Hertz1}}$ (see Fig. 8, *inset*). The constants, K_1' and K_1'', deviate from the Hertz solution for both models in thin samples. Similar to the zero-frequency case, the Tu and the Chen models agree well with each other for $\nu = 0$.

The Hertz model and its limitations

The limitations of the Hertz model are well illustrated in the measurement of the zero-frequency elastic constants of

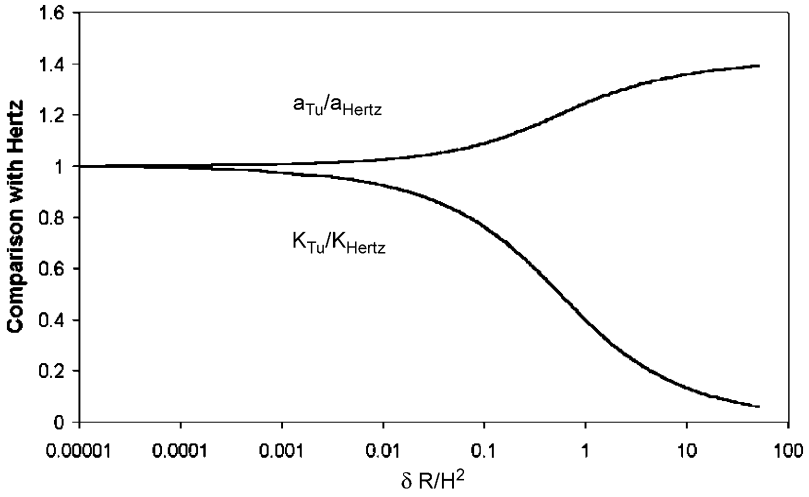

FIGURE 6 Comparison of the Tu model for nonadhered thin regions with the Hertz model. The ratios of the Chen and the Hertz model in the constant, K, and the contact radius, a, i.e., K_{Tu}/K_{Hertz} and a_{Tu}/a_{Hertz}, are plotted as a function of the square of the Hertz contact radius (δR) normalized with respect to the square of the sample height, i.e., $\delta R/h^2$. As the sample height increases, the predicted constant, K_{Tu}/K_{Hertz}, and the predicted contact radius, a_{Tu}/a_{Hertz}, approach 1, indicating that the Tu solutions converge to the Hertz solutions at large sample depths.

fibroblasts (NIH 3T3) shown in Fig. 9. The Hertz model appears to be effective only in thick regions away from the leading edge of the cell. To make this argument, two points on each fibroblast cell were chosen (see Fig. 9). One point lies near the leading edge, whereas the other lies closer to the main cell body. Near the main body of the cell, the Hertz model successfully measures the elastic constant, whereas near the leading edge the Hertz model displays an increase in the elastic modulus as the indentation increases. Thus, this simple model is not effective in all regions of the cell.

Qualitatively, we expect that a hard substrate provides support to the soft cell and will result in an apparent increase in the elastic constants. It is also possible that the thinner regions experience a higher strain due to the relatively higher compression. The magnitude of this increase depends on the thickness of the cell at the point of measurement and on the adhesion between the cell and the substrate. In nature, a cell dynamically changes its viscoelastic properties and shows spatial inhomogeneity over a cell. However, assuming a constant elastic modulus over the entire range of indentation is valid, considering the small contact area and the fast measurement time. The lateral inhomogeneity cannot affect our measurements, considering that the contact area is small; the diameter of the contact area is in the submicron range, approximately a few hundred nanometers. For thin regions, the situation is simple since there is no cytoskeletal variation perpendicular to the substrate due to the limited depth. For the thick regions where the Hertz model applies, our measurements can be affected not only by the lateral variation but also by the vertical variation. However, the recent theoretical work shows that even if a stiffer microtubule network or nucleus is underlying the actin cortex, the elastic response is dominated by the shell-like actin cortex; only if the tip presses directly on the nucleus does its high stiffness becomes relevant (R. Ananthakrishnan J. Guck, F. Wottawah, S. Schinkinger, B. Lincoln, M. Romeyke, T. Moon, and J. Käs, unpublished). This is in agreement with our findings that the elastic modulus remains constant for

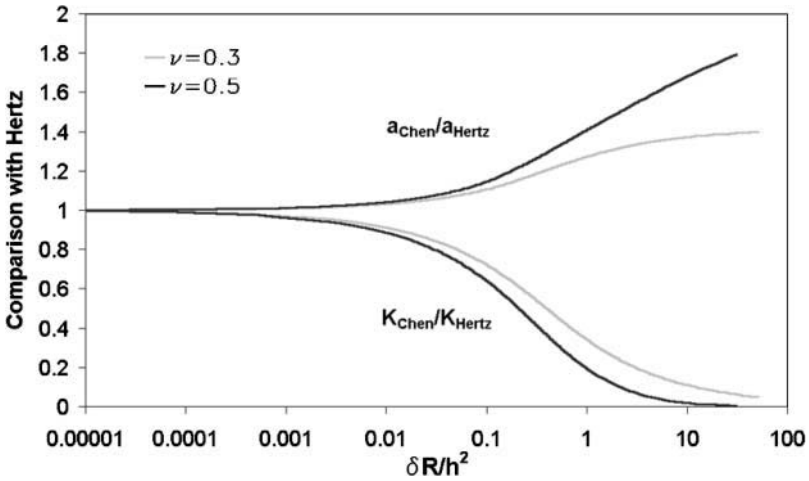

FIGURE 7 Comparison of the Chen model for adhered thin regions with the Hertz model. The ratios of the Chen and the Hertz model in the constant, K, and the contact radius, a, i.e., K_{Chen}/K_{Hertz} and a_{Chen}/a_{Hertz}, are plotted as a function of the square of the Hertz contact radius (δR) normalized with respect to the square of the sample height, i.e., $\delta R/h^2$. The values of K_{Chen}/K_{Hertz} and a_{Chen}/a_{Hertz} depend on the Poisson ratio, ν, of the material. The substrate effect is apparent at lower indentations as the Poisson ratio, ν, increases.

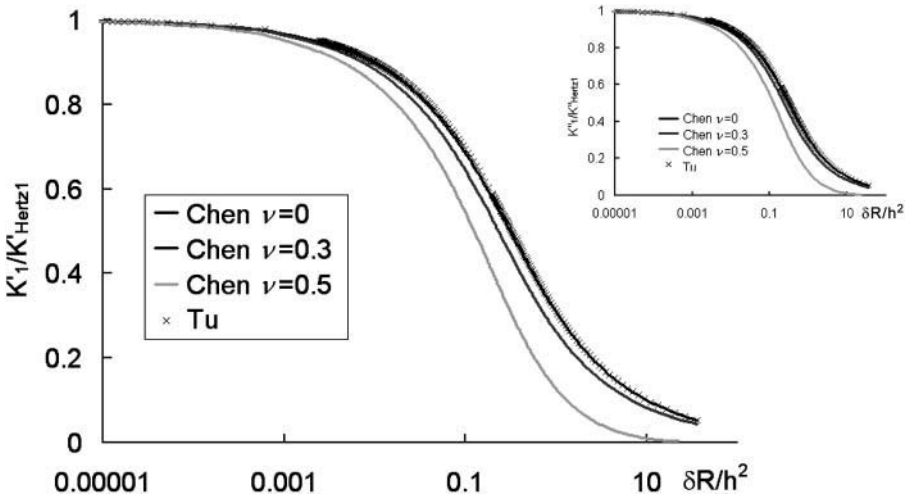

FIGURE 8 Comparison of the storage, K', and the loss modulus, K'', calculated from the Chen model with various Poisson ratios and from the Tu model. The ratios of the frequency-dependent elastic constant, $K_1'/K'_{\mathrm{Hertz1}}$, for each model are plotted as a function of the square of the Hertz contact radius normalized with respect to the square of the sample height, i.e., $\delta R/h^2$. The ratio $K_1''/K''_{\mathrm{Hertz1}}$ for each model shown in the inset displays the same relation as that of the frequency-dependent elastic constant, $K_1'/K'_{\mathrm{Hertz1}}$. In the case of a Poisson ratio of zero, the Chen and the Tu model agree with each other. At higher Poisson ratios, the Chen and the Tu model deviate significantly.

low indentations where we indent only the actin cortex and for high indentations where other cytoskeletal structures are compressed. As for the dynamical changes, the measurements are performed within a timescale that is fast with respect to cell movement. The measurement times range from 1 s to a few 10 s, which are faster than the speed of fibroblasts' movements.

Cell elasticity measurements in thin adhered regions

For very thin regions of the cell, we expect the Hertz model to be inaccurate because the substrate effects described above dominate the elastic properties. In this case the adhesive state of the plasma membrane is an important determinant. Strong adhesion between the cell membrane and the substrate will provide additional support for the cell to resist lateral deformations that release energy. In nonadherent areas, the substrate opposes the vertical deformations, but the sample remains laterally free. Thus, the effect of the substrate is expected to be less obvious in a nonadherent sample than in the adherent sample. Different areas of the cell behave either like the adhered case or the nonadhered case. Optical microscopy can provide information about which regions of a cell are adhered to the substrate. Rhodamine phalloidin binds to actin filaments in

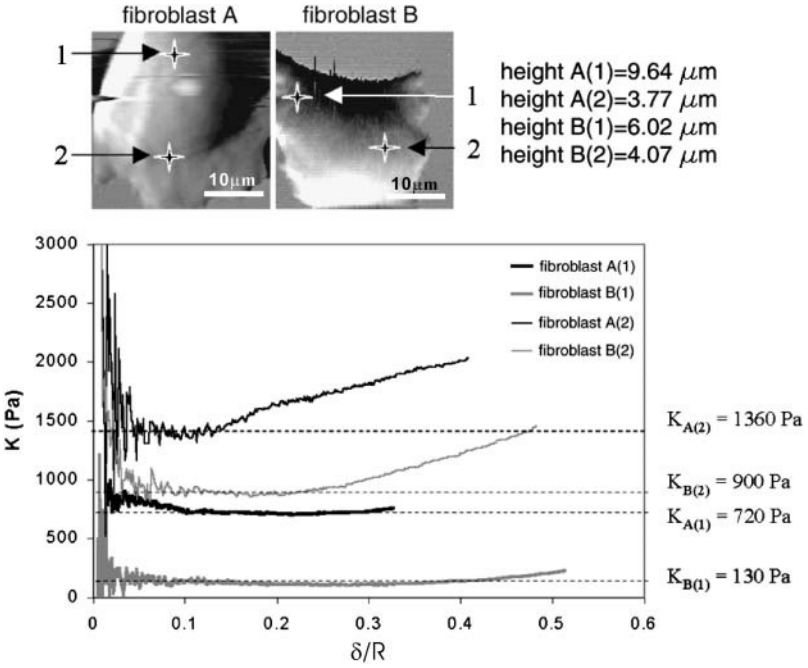

FIGURE 9 The elastic constants, K, predicted by the Hertz model. The data were taken at four points on two different NIH 3T3 fibroblasts (fibroblasts A and B). The points of measurement are indicated by a star on error-mode images of the cells. The elastic constants, K, are plotted as a function of the relative indentation depth, δ/R. The values of K and the heights of each point are shown. The Hertz model provides reliable data for thick areas of the cell.

the cell and indicates regions of high actin filament density. Motile fibroblasts (NIH 3T3) show a higher actin density relatively near the leading edge (see Fig. 10 *A*). In this region, the focal adhesions connected to the actin cytoskeleton are closely spaced and indicate that the sample is well adhered. In contrast, further away from the leading edge, the densities of the filament and focal adhesion points decrease. Thus, the sample should behave like the nonadhered case. Similarly, in images obtained by reflection interference contrast microscope, the darker points indicate the regions of strong adhesion at the leading edge of the lamellipodium (see Fig. 10 *B*). Therefore, the leading edge should follow the Chen model whereas regions away from the leading edge will be closer to the Tu model. Indeed, such assignments of the well-adhered and nonadhered regions based on optical microscopy are consistent with the force measurements performed using AFM.

Considering first the leading edge, we reanalyzed the data of fibroblast A (NIH 3T3) in Fig. 9 taken at point 2 using both the Chen model with various Poisson ratios and the Tu model. At point 2, the total thickness of the sample with respect to the substrate is 3.8 μm. The results of these measurements are shown in Fig. 11. The Hertz and the Tu models clearly fail to predict an elastic constant. The Chen model with a Poisson ratio of 0.4 yields the most constant elastic modulus over the full range of indentations. This observation is commensurate with the optical data, which show a dense actin network in this region, indicating many opportunities for adhesion. The high Poisson ratio indicates that the actin gel in this region is highly cross-linked.

The Chen model is successful in the very thin regions near the edge of fibroblasts. In these regions the cell is generally well adhered to the substrate and is <1 μm thick. An example of data for an NIH 3T3 fibroblast obtained in this region is shown in Fig. 12. The relative indentations were in this instance a significant portion of the total height of the sample, $h = 790$ nm. Even so, the Chen model returns a constant value of the elastic modulus of 1.6 kPa and a Poisson ratio of 0.5. In contrast, no portion of the curve from the Hertz model is truly constant. The data obtained from the Chen model confirm that the leading edge of a fibroblast is strongly adhered and supported by a strongly cross-linked intracellular polymer network.

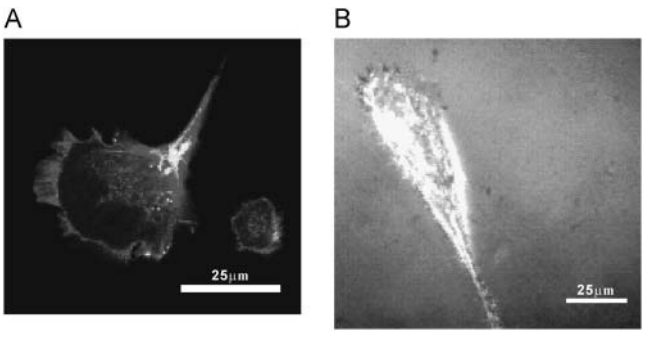

FIGURE 10 Optical images of motile NIH 3T3 fibroblasts. The region close to the leading edge is clearly adhered. (*A*) An NIH 3T3 fibroblast fixed and stained with rhodamine phalloidin. The fluorescent areas show high actin filament density. (*B*) Reflection interference contrast image of an NIH 3T3 fibroblast. The dark spots near the leading edge indicate that these regions adhere well to the substrate.

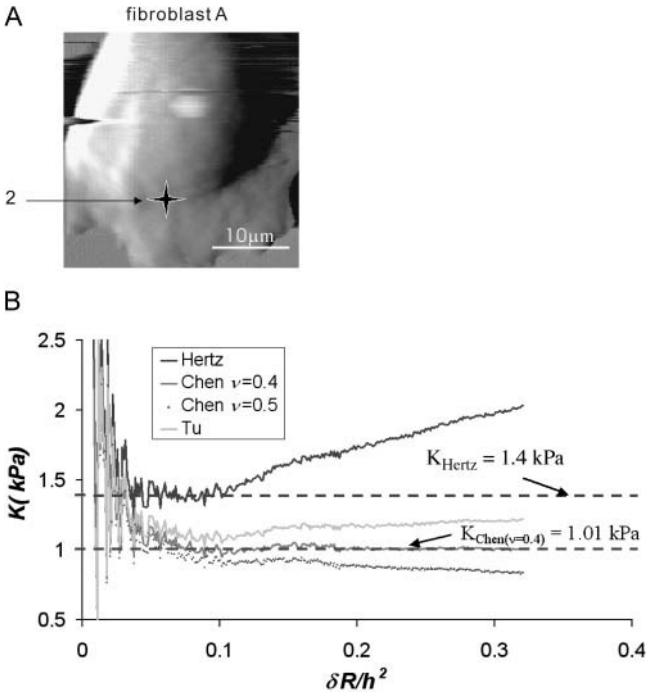

FIGURE 11 Zero-frequency elastic properties of the leading edge of an NIH 3T3 fibroblast. (*A*) Error-mode image of an NIH 3T3 fibroblast. The star indicates the point of measurements close to the leading edge. (*B*) Plot of the elastic constant, K_0 vs. $\delta R/h^2$, as calculated by the Hertz, Tu, and Chen models for a Poisson ratio of 0.4 and 0.5. The best results are obtained with the Chen model for a Poisson ratio of 0.4, confirming that the leading edge adheres to the underlying substrate and shows a strong elastic response, which is typical for a highly cross-linked polymer gel.

Cell elasticity measurements in thin nonadhered regions

In the case that the cell is poorly adhered, the Chen model fails for reasonable values of the Poisson ratio. This effect is demonstrated with point 3 on the same cell of Fig. 9 (see Fig. 13). The plot of the elastic values of K as a function of the quantity, $\delta R/h^2$, shows that the Chen model with various Poisson ratios is ineffective. In this case, the Tu model is effective in predicting an elastic constant at deep indentations, whereas the other models fail. Fig. 13 demonstrates an additional effect seen in cells. At very low indentations, the Tu model is not as effective and the Hertz model seems to be predicting a somewhat higher elastic constant. This variation may be due to uncertainty in the contact point. As

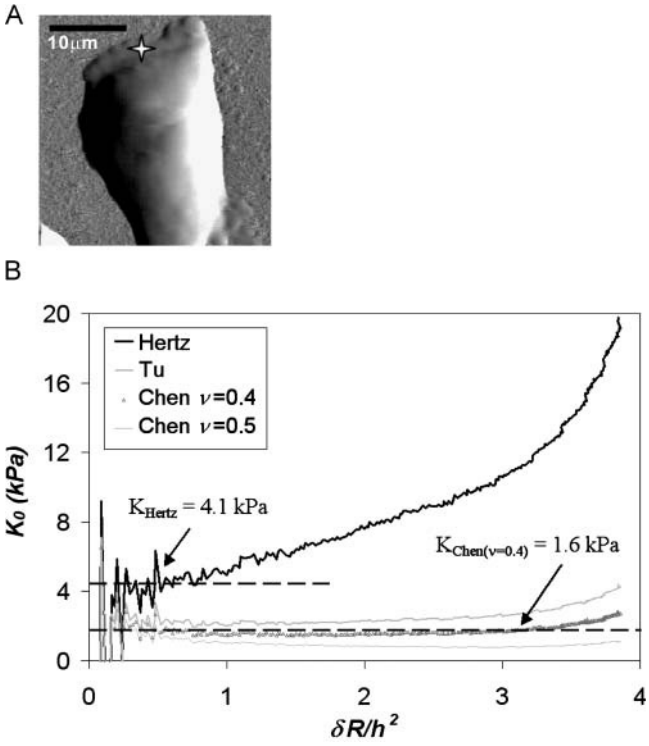

FIGURE 12 Demonstration of the effectiveness of the Chen model on extremely thin adhered regions of an NIH 3T3 fibroblast. (*A*) Error-mode image of an NIH 3T3 fibroblast. The zero-frequency elastic data were taken at the marked point. The height of this point, h, is 790 nm. (*B*) K_0 vs. $\delta R/h^2$ plotted for the Hertz, the Tu, and the Chen model for Poisson ratios of 0.4 and 0.5. The best result is obtained for the Chen model for a Poisson ratio of 0.4, confirming the appropriateness of this model for very thin, and adhered regions of a cell.

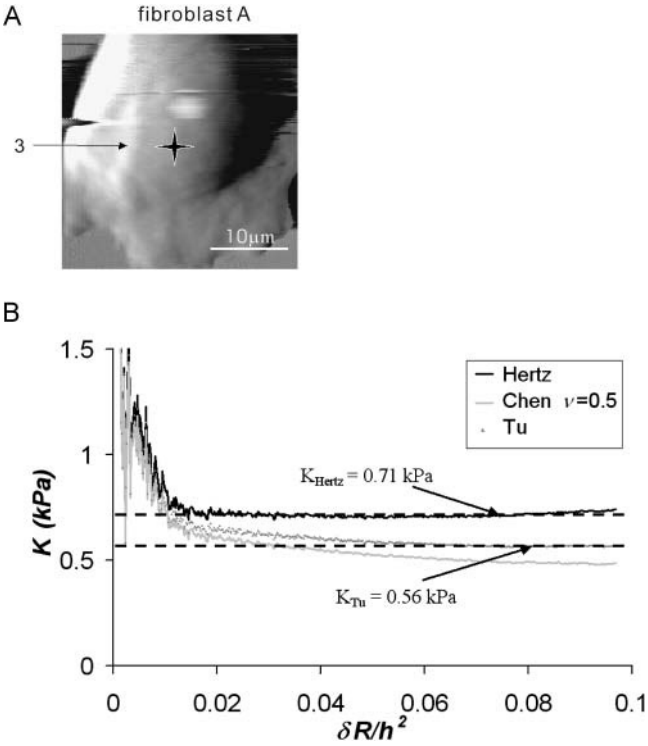

FIGURE 13 Measuring the zero-frequency elastic properties of an NIH 3T3 fibroblast at a point further back from the well-adhered leading edge. (*A*) Error-mode image of the NIH 3T3 fibroblast. The point of measurement is marked by a star. The height of this point is 9.81 μm. (*B*) K_0 vs. $\delta R/h^2$ plotted for the Hertz model, the Chen model with a Poisson ratio of 0.5, and the Tu model. For deep indentations only the Tu model leads to satisfactory results.

predicted from the numerical calculations, the apparent elastic modulus from the Hertz model exceeds the modulus from the Tu model (see Fig. 6). We also observed in the above example that the difference between the Hertz and the Tu constant is ~25% at low indentations (see Fig. 13). Under the assumption that a sole elastic modulus can be obtained from our measurements, the Tu model is most appropriate since it provides the constant elastic modulus at high indentations. Another potential explanation would suggest that the Hertz model works at low indentations where the tip probes the cytoskeleton directly underlying the plasma membrane although the Tu model is more effective at higher indentations where the tip probes the entire cytoskeleton.

The Hertz model generally overestimates the elastic constant with a bigger error in regions that are well adhered, even though the height of the sample may be ~30 times larger than the indentation. The Chen model predicts an elastic constant of 1.01 kPa for the thicker sample, whereas the Hertz model predicts an approximate constant of 1.4 kPa at low indentation, representing a difference of nearly 40% (see Fig. 11). Although both the Tu and the Chen models are relatively simple, in that they assume a sole elastic constant with respect to the indentation, they are extremely effective over the thin regions of the cell.

Viscoelastic behavior in thin regions

The viscoelastic values at 80 Hz were measured for an NIH 3T3 fibroblast at the point indicated in the inset of Fig. 14. Neither the Hertz nor the Tu model is effective in this case at predicting the two parts of the viscoelastic constant, K' and K''. Only the Chen model with a Poisson ratio of 0.5 shows a constant behavior for K' and K'' over a wide range of indentations. The storage modulus, $K' \sim 1.4$ kPa, is comparable to our measurements of the zero-frequency elastic constant, K, obtained at the leading edge. The viscous contribution, i.e., the loss modulus, K'', is ~860 Pa. The viscosity clearly represents an important component of the total mechanical properties of the cell. However, since $K' > K''$, the cell displays an elastic behavior similar to polymer gels in the rubber plateau regime. From the strong elastic

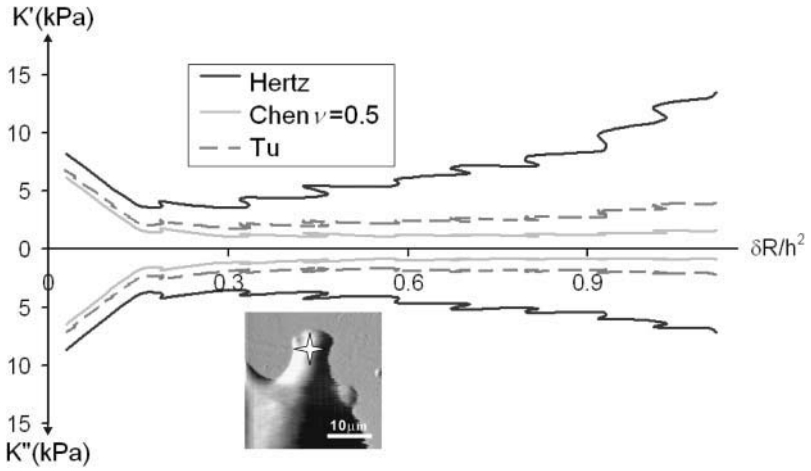

FIGURE 14 The storage, K', and loss constant, K'', for a frequency of 80 Hz plotted as a function of $\delta R/h^2$. The measurement point is marked as a star at the error-mode image of the NIH 3T3 fibroblast. The height of this point is 0.6 μm. In the case of the Hertz and the Tu model, K' and K'' deviate from a constant value as the indentation, $\delta R/h^2$, increases. However, the Chen model with a Poisson ratio of 0.5 shows a constant behavior over an extended range of indentations. The resulting storage modulus, $K' = 1.40 \pm 0.26$ kPa, is higher than the loss modulus, $K'' = 0.86 \pm 0.05$ kPa. Thus, the sample behaves elastically.

component and the effectiveness of the Chen model, we can conclude that this region of the cell, shown in the inset of Fig. 14, is well adhered to the substrate and strongly cross-linked. This measurement is done at the point relatively near the edge of the cell and thus the noted adhesion is in agreement with our previous optical results (see Fig. 10 *B*).

Viscoelastic data of the same cell in Fig. 14 taken at frequencies ranging from 80 to 300 Hz are shown in Fig. 15. The Hertz model is not suitable to predict the loss and storage moduli for this thin sample ($h = 600$ nm) and the Tu model also fails as shown in Fig. 14. The Chen model with a Poisson ratio of 0.5 efficiently alleviates the substrate effect. Thus, we were able to evaluate the viscoelastic moduli in an analogous manner to the zero-frequency data with the

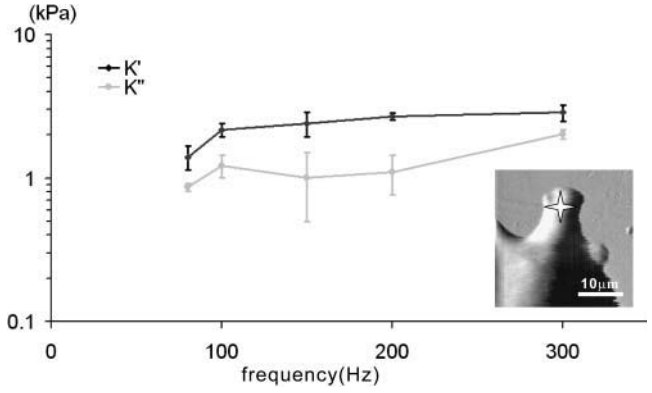

FIGURE 15 The storage, K', and loss constant, K'', plotted as a function of the frequency (80–300 Hz) for an NIH 3T3 fibroblast. The Chen model with a Poisson ratio of 0.5 was most effective to alleviate the strong substrate effect associated with the deep indentation as shown in Fig. 14. The data are taken at the point indicated in the error-mode image of the fibroblast. The height of this point is ~0.6 μm. The constants, K' and K'', at each frequency were obtained as an average over the regions, in which the plot of K' and K'' vs. $\delta R/h^2$ shows a constant behavior over an extended range of indentations (see Fig. 14). The error bar indicates the standard deviation over these regions. The data show that there is a rubber plateau region <300 Hz.

premise that this point of the cell is well adhered to the substrate. Between 80 Hz and 300 Hz the storage modulus, K', exceeds the loss modulus, K'', for the Chen model. Thus, the sample shows an elastic, rubber plateau-like behavior. The storage modulus ranges from 1400 Pa to 2870 Pa over the observed frequency range. A transition from the plateau regime to an internal dynamic regime does not occur within this frequency range (80–300 Hz), although the viscous component approaches the elastic component at high frequency, indicating the onset of this transition (see data taken at 300 Hz). The onset of the internal dynamics regime at such high frequencies implies the presence of a cross-linked actin network in vivo, since the onset occurs earlier in a non-cross-linked, solely entangled network (Morse, 1998). This cross-linking is also consistent with our finding that the Chen model with a Poisson ratio of 0.5 is most effective in this region. In addition, the transition frequency to an internal dynamics regime depends on the length of actin filaments. Shorter filaments like those found in a cell show a higher transition frequency. The numerical data by Morse predicts the transition at 160 Hz for non-cross-linked entangled filaments of 17 μm in length, which is much longer than cellular actin filaments (<1 μm). These measured viscoelastic constants and the Poisson ratio of 0.5 lead to shear moduli of $G' = 350$–715 Pa and $G'' = 215$–500 Pa for the storage and the loss moduli, respectively. Since malignantly transformed fibroblasts exhibit a drastically reduced cytoskeleton—actin decreases by ~30%—it is expected that the strength is drastically lowered in the elastic plateau regime. *H-ras*-transformed fibroblasts are a typical example of malignantly transformed fibroblasts. The data taken from an *H-ras* fibroblast are shown in Fig. 16. The data were best analyzed by the Chen model with the Poisson ratio of 0.5, which makes the data comparable to the normal fibroblast (NIH 3T3) studied in Fig. 15. The frequency-dependent measurement again displays an elastic plateau regime. However, the elastic strength of this plateau is significantly

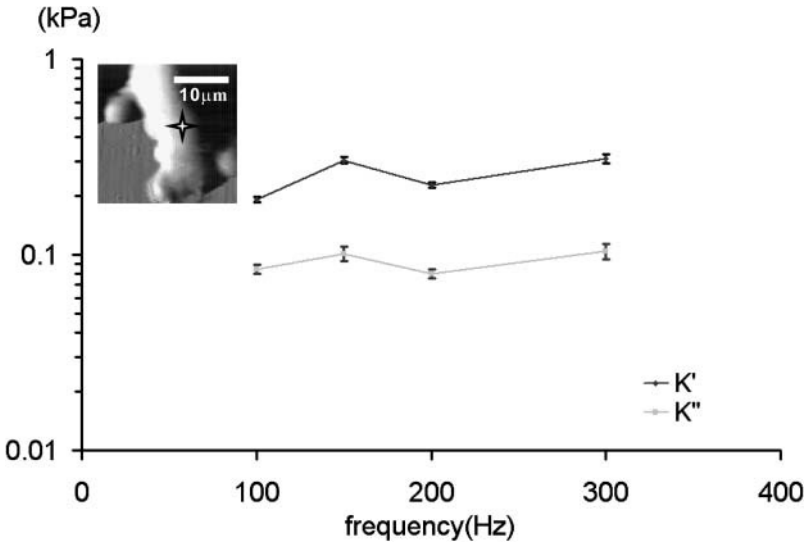

FIGURE 16 The storage, K', and loss constant, K'', plotted as a function of the frequency (80–300 Hz) for an *H-ras*-transformed fibroblast. The Chen model with a Poisson ratio of 0.5 is used to evaluate the viscoelastic modulus. The data were taken at the point indicated in the error-mode image of the fibroblast. The height of this point is ~4.1 μm. In the studied frequency regime the adhered region of the *H-ras*-transformed fibroblast displays an elastic plateau, which is significantly lower than the plateau for the NIH 3T3 fibroblast shown in Fig. 15.

lower. The shear moduli were determined to be $G' = 50$–100 Pa and $G'' = 20$–30 Pa. Both are significantly lower than values for the normal NIH 3T3 fibroblasts. Our data illustrate that the local viscoelastic signature of cells can be used as a cell marker to distinguish cells by their cytoskeletal phenotype. As a rule of thumb the elastic strength of a cell increases with its degree of differentiation. The measured plateau moduli can only be achieved by cross-linked actin networks and not by entangled actin networks (Morse, 1998). Considering that physiologic actin concentrations is 10–20 mg/ml and only a fraction of actin filaments are cross-linked by transient cross-linking proteins, actin networks can only achieve the structural strength measured in our experiments if most of the cellular actin is concentrated in the lamellipodial regions that we investigated (Ananthakrishnan, 2003; Wachsstock et al., 1994).

In conclusion, the appropriate model treating the viscoelastic indentation of a soft sample with finite thickness is key to successfully characterizing both the viscoelastic and adhesive properties of a cell. Viscoelastic data can be obtained even in very thin regions of the cell while simultaneously measuring the Poisson ratio. Besides the impact of thickness, the local adhesion of the cell has a strong effect on the apparent elastic properties of the sample. Simple models such as the Hertz model can overestimate the elastic constant in regions where the cell is well adhered. The combination of a well-defined spherical contact area and a carefully chosen model provides accurate information on a cell's or any thin sample's viscoelastic properties. The presented methods allow spatially resolved precise rheological measurements of thin soft samples such as lamellipodia of cells and block co-polymer films. Simultaneously, these methods also allow us to determine the adhesive state of the sample with respect to the underlying substrate. In thin adhered samples the method uniquely determines the Poisson ratio in addition to the shear modulus providing the most complete viscoelastic information. Our results show that the region relatively close to the leading edge of motile fibroblasts strongly adheres to the substrate. The viscoelastic signature of the lamellipodium strongly resembles those of cross-linked polymer networks such as actin gels. Thus the structural strength of the leading edge of a lamellipodium is determined by a cross-linked network of short actin filaments that are strongly coupled to the substrate by focal adhesions. The data demonstrate that our method is ideally suited for measuring the frequency-dependent elastic modulus, the Poisson ratio, and the adhesive state of the lamellipodium.

APPENDIX

Here we summarize the adaptation of the calculations originally presented by Tu and co-worker and Chen and co-worker to our AFM measurements (Tu and Gazis, 1964; Chen, 1971; Chen and Engel, 1972). Since we consider the loading over a circular region of radius, a, caused by the modified spherical AFM tip, it is more convenient to use the cylindrical coordinates (r, θ, z). The total stress distribution applied by the spherical tip, $p(r)$, can be described by the sum over a series of partial pressure distributions, $q_i(r)$, which is approximated in Eq. A1. The normalization factors, p_i, must be calculated for each $q_i(r)$ and included in the total force calculation, as

$$p(r) = \frac{G\delta}{a}\sum_{i=1}^{N} p_i q_i(r), \tag{A1}$$

with

$$q_i(r) = \left(1 - \frac{r^2}{a^2}\right)^{i-1/2}.$$

The indentation depth, δ, the shear modulus, G, and the radius of the contact region, a, are related in these equations. The stress distribution relates to the displacement, $u(r)$, at each point in the contact area as

$$u(r) = \sum_{i=1}^{N} u_i(r), \tag{A2}$$

with

$$u_i(r) = \delta\, p_i w_i(r).$$

Here, $w_i(r)$ is defined as a normalized displacement and is related to the corresponding partial pressure distribution, $q_i(r)$, which appears later in Eq. A5.

For the elasticity problem, in which the shearing stress vanishes at all points in a hard substrate, stresses and displacements are expressed in terms of two harmonic functions, F and Z, in the form of Fourier-type integrals (Green and Zerna, 1954). As mentioned earlier, assuming the axially symmetric loading allows us to use cylindrical coordinates. So the integrand $e^{i(mx+ny)}$ of the Fourier-type integrals can be replaced with the spherical Bessel function $J_0(\alpha r)$ as

$$\begin{cases} F = \int_0^\infty \frac{1}{\alpha^2}(Ae^{-\alpha z} + Be^{\alpha z})\overline{p}(\alpha)J_0(\alpha r)\alpha\, d\alpha \\ Z = \int_0^\infty \frac{1}{\alpha}(Ce^{-\alpha z} + De^{\alpha z})\overline{p}(\alpha)J_0(\alpha r)\alpha\, d\alpha \end{cases}. \tag{A3}$$

Here α is defined as $(m^2 + n^2)^{1/2}$ and $\overline{p}(\alpha)$ is the Fourier transform of the total pressure distribution, $p(r)$,

$$\overline{p}(\alpha) = \int_0^a p(r)J_0(\alpha r)r\, dr. \tag{A4}$$

Similarly the N normalized displacements, $w_i(r)$, can be written as

$$aw_i(r) = G\int_0^\infty \overline{u}_n(\alpha h)\overline{q}_i(\alpha)J_0(\alpha r)d\alpha, \tag{A5}$$

with

$$\overline{q}_i(\alpha) = \int_0^a q_i(r)J_0(\alpha r)r dr.$$

The N normalized displacements are calculated through numerical integration of the pressure distribution over the surface of contact. The function $\overline{u}_n(\alpha h)$ is determined by the boundary conditions of the adhered and nonadhered regions. The detailed boundary conditions and the exact forms of $\overline{u}_n(\alpha h)$ for the Tu and the Chen models are presented in the next two sections. The subscript, n, denotes the normal component with respect to the hard substrate. For the calculation of the elastic values, the spherical Bessel function, $J_0(\alpha r)$, as well as the total stress distribution, $p(r)$, can be approximated as a series of Legendre polynomials.

The spherical probe shape of the tip can be modeled as a parabolic indenter, which results in a surface indentation as

$$u_0(r) = \delta - \frac{r^2}{2R}. \tag{A6}$$

The real surface indentation function, $u(r)$, has the properties of being a smooth and continuous function, which vanishes at the edge of the tip and is stationary at the center of the tip. The error resulting from the approximation of a parabolic probe can be rewritten as a function, $\varepsilon(r)$,

$$\varepsilon(r) = \frac{1}{\delta}(u_0(r) - u(r)), \tag{A7}$$

$$\varepsilon(r) = 1 - \frac{r^2}{2R\delta} - \sum_{i=1}^{N} p_i w_i(r). \tag{A8}$$

Using the method of least-squares, one needs to minimize the integral of the square of the error over the contact area,

$$I_L = \frac{1}{a^2}\int_0^a r\varepsilon^2(r)dr. \tag{A9}$$

The above error integral is minimized when the following conditions are fulfilled:

$$\frac{\partial I_L}{\partial(\delta/a)} = 0, \quad \frac{\partial I_L}{\partial p_i} = 0, \quad (i = 1 \ \ldots N). \tag{A10}$$

These conditions, which result in $N + 1$ equations, allow us to determine the radius of the contact area, a, and the normalization factors of the partial pressure distribution, p_i. These equations have the form of

$$\begin{cases} 3 - \frac{a^2}{R\delta} - \frac{12}{a^4}\int_0^a r^3 \sum_{i=1}^{N} p_i w_i(r)dr = 0 \\ \int_0^a r w_j(r)\left[1 - \frac{r^2}{2R\delta} - \sum_{i=1}^{N} p_i w_i(r)\right]dr = 0, \\ \qquad (i,j = 1,2,3,\ldots .N) \end{cases}. \tag{A11}$$

To complete the numerical integration of the above equations, all the integrals must be rewritten in terms of equivalent integrals over the range [0,1] . For this purpose, we introduced three normalized quantities, r', h', and α', corresponding to r/a, h/a, and αa, respectively. The integrals converge more quickly if the half-space solution for a given pressure distribution, $\overline{u}_n^H(\alpha h)$, is subtracted from $w_i(r)$ before integration and then added back later. So Eq. A5 can be rewritten as

$$aw_i(r) - aw_i^H = G\int_0^\infty [\overline{u}_n(\alpha h) - \overline{u}_n^H(\alpha h)]\overline{q}_i(\alpha)J_0(\alpha r)d\alpha, \tag{A12}$$

with

$$aw_i^H = G\int_0^\infty \overline{u}_n^H(\alpha h)\overline{q}_i(\alpha)J_0(\alpha r)d\alpha.$$

The results of the numerical integration provide coefficients, $w_i(r)$, for the equations shown in Eq. A11. Consequently, these equations can be solved to determine the values of p_i and δ/a, where δ is experimentally measured. The other experimentally measurable quantity is the deforming force, which is related to the integral of the total pressure distribution over the contact area, as

$$f_{bead} = \int_0^a p(r)2\pi r\, dr. \tag{A13}$$

With the relationship of shear modulus, G, and the Young's modulus, E, which is given by $G = E/(2 + 2\nu)$, the deforming force is

$$f_{bead} = \frac{\pi E}{1+\nu}\delta a \sum_{i=1}^{N} \frac{p_i}{1+2i}. \tag{A14}$$

Here, the value, p_i, is a function of the Poisson ratio, ν. In the following we consider our two boundary conditions: the nonadhered and adhered regions.

Nonadhered thin regions of cells—the Tu model

The general forms of the displacements and the stresses, i.e., $\overline{u}_n(\alpha z)$, $\overline{u}_s(\alpha z)$,$\overline{\sigma}_n(\alpha z)$, and $\overline{\sigma}_s(\alpha z)$, are defined as

$$\begin{cases} 2G\overline{u}_n(\alpha z) = -[A + (\alpha z + k)C]e^{-\alpha z} + [B + (\alpha z - k)D]e^{\alpha z} \\ 2G\overline{u}_s(\alpha z) = -[A + \alpha z C]e^{-\alpha z} - [B + \alpha z D]e^{\alpha z} \\ \overline{\sigma}_n(\alpha z) = [A + (\alpha z + 2 - 2\nu)C]e^{-\alpha z} + [B + (\alpha z - 2 + 2\nu)D]e^{\alpha z} \\ \overline{\sigma}_s(\alpha z) = [A + (\alpha z + 1 - 2\nu)C]e^{-\alpha z} - [B + (\alpha z - 1 + 2\nu)D]e^{\alpha z} \end{cases}. \tag{A15}$$

Here, k is equal to (3–4ν), where ν is the Poisson's ratio. The subscripts, n and s, correspond to the normal and tangential components with respect to the hard substrate. For the nonadhered case, at the center of the layer there is no vertical displacement as would be expected for an infinitely hard substrate ($\overline{u}_n(0) = 0$). However, the lateral displacement is unconstrained and there is no lateral stress on the rigid surface ($\overline{\sigma}_s(0) = 0$). The vertical stresses at the sample surface are functions of the indenter shape ($\overline{\sigma}_n(h) = 1$). The indenter is frictionless with respect to the sample ($\overline{\sigma}_s(h) = 0$). These four conditions are enough to determine $\overline{u}_n(\alpha h)$ in Eq. A15. $\overline{u}_n(\alpha h)$ is a simple function of the height of the layer, h, and the Poisson ratio, ν, as

$$G\overline{u}_n(\alpha h) = \frac{2(1-\nu)\sinh^2(\alpha h)}{\sinh(2\alpha h) + 2\alpha h}. \tag{A16}$$

Since the Poisson ratio appears in a single factor, (*1–*ν), of $\overline{u}_n(\alpha h)$, it can be factored out and grouped with the Young's modulus in the Tu model as was done for the Hertz model.

The half-space solution for a given pressure distribution was solved by Chen and co-worker (Chen, 1971; Chen and Engel, 1972). The displacements in the corresponding uniform half-space problem are

$$G\overline{u}_n^H = (1-\nu) = (k+1)/4; \tag{A17}$$

$$Gw_i^H = -(1-\nu)a\frac{\pi(2n-1)(2n-3)\ldots..(3)(1)}{2^{n+1}n!} \times {}_2F_1(1/2, -n; 1; \frac{r^2}{a^2}). \tag{A18}$$

Adhered thin regions of cells—the Tu model

To simplify the numerical calculations, Chen redefined the coefficients as

$$\begin{cases} Ae^{-\alpha h/2} = A'e^{-2\alpha h} \\ Be^{\alpha h/2} = \alpha h/2 - (1-2\nu) + B'e^{-2\alpha h} \\ Ce^{-\alpha h/2} = C'e^{-2\alpha h} \\ De^{\alpha h/2} = -1 + D'e^{-2\alpha h} \end{cases}. \tag{A19}$$

Based on these variables, the corresponding quantities from Eq. A15 became

$$\begin{cases} 2G\left[\overline{u}_n(\alpha z) - \overline{u}_n^H\left(\frac{\alpha h}{2}\right)\right]e^{2\alpha h} = -[A' + (\alpha z + k)C']e^{-\alpha(z-h/2)} + [B' + (\alpha z - k)D']e^{\alpha(z-h/2)} \\ 2G\left[\overline{u}_s(\alpha z) - \overline{u}_s^H\left(\frac{\alpha h}{2}\right)\right]e^{2\alpha h} = -[A' + \alpha z C']e^{-\alpha(z-h/2)} - [B' + \alpha z D']e^{\alpha(z-h/2)} \\ \left[\overline{\sigma}_n(\alpha z) - \overline{\sigma}_n^H\left(\frac{\alpha h}{2}\right)\right]e^{2\alpha h} = [A' + (\alpha z + 2 - 2\nu)C']e^{-\alpha(z-h/2)} + [B' + (\alpha z - 2 + 2\nu)D']e^{\alpha(z-h/2)} \\ \left[\overline{\sigma}_s(\alpha z) - \overline{\sigma}_s^H\left(\frac{\alpha h}{2}\right)\right]e^{2\alpha h} = [A' + (\alpha z + 1 - 2\nu)C']e^{-\alpha(z-h/2)} - [B' + (\alpha z - 1 + 2\nu)D']e^{\alpha(z-h/2)} \end{cases}. \tag{A20}$$

Now, the sample is rigidly bound to the substrate and thus the tension is only freely released at the surface. The boundary conditions are that the lateral and vertical displacements at the surface of the substrate are zero ($\overline{u}_s(-2/h) = 0$, $\overline{u}_n(-2/h) = 0$). The vertical and lateral stresses at the probe-sample interface are the same as those used in the Tu model ($\overline{\sigma}_n(h/2) = 1$, $\overline{\sigma}_s(h/2) = 0$). Applying these boundary conditions to each equation in Eq. A20, the coefficients are calculated to be

$$\begin{cases} C' = [1 + 2\alpha h + ke^{-2\alpha h}]/\psi(\alpha) \\ D' = [2\alpha h(1 + 2\alpha h) + k^2 + ke^{-2\alpha h}]/\psi(\alpha) \\ A' = -[(\alpha h + k)C' - D']/2 \\ B' = -[C' + (\alpha h - k)D']/2 \end{cases}, \tag{A21}$$

where $\psi(\alpha)$ is defined to be

$$\psi(\alpha) = k + [k^2 + (2\alpha h)^2 + 1]e^{-2\alpha h} + ke^{-4\alpha h}, \tag{A22}$$

so the full form of $\overline{u}_n(\alpha h/2)$ is given by

$$\overline{u}_n\left(\frac{\alpha h}{2}\right) - \overline{u}_n^H\left(\frac{\alpha h}{2}\right) = -\frac{2k(1+k)e^{-4\alpha h} + [1 + 4\alpha h(1+\alpha h) + k + k^2 + k^3 + 4k\alpha h(1+\alpha h)]e^{-2\alpha h}}{4[k + (k^2 + (2\alpha h)^2 + 1)e^{-2\alpha h} + ke^{-4\alpha h}]}. \tag{A23}$$

Note that for the rigidly adhered model, we substitute $\overline{u}_n(\alpha h) - \overline{u}_n^H(\alpha h)$ in Eq. A12 with $\overline{u}_n(\alpha h/2) - \overline{u}_n^H(\alpha h/2)$, because the coordinate is defined differently (see Fig. 1).

We thank Dr. F. Mackintosh and Dr. P. Barbara for helpful discussions.

This research was supported by a National Institutes of Health grant (1R29AR45008-01). Additional funding was provided by the Integrative Graduate Education and Research Traineeship program administered by Dr. R. Richards-Kortum through a National Science Foundation grant (DGE-9870653). J. K. was also supported by the Wolfgang-Paul prize of the Alexander von Humboldt Foundation.

REFERENCES

A-Hassan, E., W. F. Heinz, M. D. Antonik, N. P. D'Costa, S. Nageswaran, C. Schoenenberger, and J. H. Hoh. 1998. Relative microelastic mapping of living cells by atomic force microscopy. *Biophys. J.* 74:1564–1578.

Amblard, F., A. C. Maggs, B. Yurke, A. N. Pargellis, and S. Leibler. 1996. Subdiffusion and anomalous local viscoelasticity in actin networks. *Phys. Rev. Lett.* 77:4470–4473.

Ananthakrishnan, R. 2003. On the structural response of eukaryotic cells. PhD thesis. University of Texas at Austin, Austin, TX.

Biot, M. A. 1935. Effect of certain discontinuities on the pressure distribution in a loaded soil. *Physics.* 6:367–375.

Borisy, G. G., and T. M. Svitkina. 2000. Actin machinery: pushing the envelope. *Curr. Opin. Cell Biol.* 12:104–112.

Burmister, D. M. 1945. The general theory of stresses and displacements in layered (soil) systems. *J. Appl. Phys.* 16:89–94,126–127,296–302.

Butt, H. J., and M. Jaschke. 1995. Calculation of thermal noise in atomic force microscopy. *Nanotechnology.* 6:1–7.

Chen, W. T. 1971. Computation of stresses and displacements in a layered elastic medium. *Int. J. Eng. Sci.* 9:775–800.

Chen, W. T., and P. A. Engel. 1972. Impact and contact stress analysis in multilayer media. *Int. J. Solids Struct.* 8:1257–1281.

Dembo, M., and Y.-L. Wang. 1999. Stresses at the cell-to-substrate interface during locomotion of fibroblasts. *Biophys. J.* 76:2307–2316.

Dimitriadis, E. K., F. Horkay, J. Maresca, B. Kachar, and R. S. Chadwick. 2002. Determination of elastic moduli of thin layers of soft material using the atomic force microscope. *Biophys. J.* 82:2798–2810.

Discher, D. E., N. Mohandas, and E. A. Evans. 1994. Molecular maps of red cell deformation: hidden elasticity and in situ connectivity. *Science.* 266:1032–1035.

Domke, J., and M. Radmacher. 1998. Measuring the elastic properties of thin polymer films with the atomic force microscope. *Langmuir.* 14:3320–3325.

Eichinger, L., B. Koppel, A. A. Noegel, M. Schleicher, M. Schliwa, K. Weijer, W. Witke, and P. A. Janmey. 1996. Mechanical perturbation elicits a phenotypic difference between *Dictyostelium* wild-type cells and cytoskeletal mutants. *Biophys. J.* 70:1054–1060.

El-Sherbiney, M. G. D., and J. Halling. 1976. The Hertzian contact of surfaces covered with metallic film. *Wear.* 40:325–337.

Elson, E. L. 1988. Cellular mechanics as an indicator of cytoskeletal structure and function. *Annu. Rev. Biophys. Biophys. Chem.* 17:397–430.

Evans, E., and A. Yeung. 1989. Apparent viscosity and cortical tension of blood granulocytes determined by micropipette aspiration. *Biophys. J.* 56:151–160.

Goldmann, W. H., R. Galneder, M. Ludwig, W. M. Xu, E. D. Adamson, N. Wang, and R. M. Ezzell. 1998. Differences in elasticity of vinculin-deficient F9 cells measured by magnetometry and atomic force microscopy. *Exp. Cell Res.* 239:235–242.

Green, A. E., and W. Zerna. 1954. Theoretical Elasticity. Oxford University Press, London.

Guck, J., R. Ananthakrishnan, T. J. Moon, C. C. Cunningham, and J. Käs. 2000. Optical deformability of soft biological dielectrics. *Phys. Rev. Lett.* 84:5451–5454.

Hénon, S., G. Lenormand, A. Richert, and F. Gallet. 1999. A new determination of the shear modulus of the human erythrocyte membrane using optical tweezers. *Biophys. J.* 76:1145–1151.

Landau, L. D., and E. M. Lifshitz. 1959. Theory of Elasticity. Pergamon Press, Oxford, UK. 30–36.

Lekka, M., P. Laidler, D. Gil, J. Lekki, Z. Stachura, and A. Z. Hrynkiewicz. 1999. Elasticity of normal and cancerous human bladder cells studied by scanning force microscopy. *Eur. Biophys. J.* 28:312–316.

Lelièvre, J. C., C. Bucherer, S. Geiger, C. Lacombe, and V. Vereycken. 1995. Blood cell biomechanics evaluated by the single cell micromanipulation. *J. Phys. III.* 5:1689–1706.

Mahaffy, R. E., C. K. Shih, F. C. MacKintosh, and J. Käs. 2000. Scanning probe-based frequency-dependent microrheology of polymer gels and biological cells. *Phys. Rev. Lett.* 85:880–883.

Morse, D. C. 1998. Viscoelasticity of concentrated isotropic solutions of semiflexible polymers. 1. Model and stress tensor. 2. Linear response. *Macromolecules.* 31:7030–7067.

Ogilvy, J. A. 1993. A parametric elastic model for indentation testing of thin films. *J. Phys. D. Appl. Phys.* 26:2123–2131.

Pantaloni, D., C. Le Clainche, and M. F. Carlier. 2001. Mechanism of actin-based motility. *Science.* 292:1502–1506.

Petersen, N. O., W. B. McConnaughey, and E. L. Elson. 1982. Dependence of locally measured cellular deformability on position on the cell, temperature and cytochalasin B. *Proc. Natl. Acad. Sci. USA.* 79:5327–5331.

Popov, G. I. 1962. The contact problem of the theory of elasticity for the case of a circular area of contact. *PMM.* 26:207–225.

Radmacher, M., M. Fritz, C. M. Kacher, J. P. Cleveland, and P. K. Hansma. 1996. Measuring the viscoelastic properties of human platelets with the atomic force microscope. *Biophys. J.* 70:556–567.

Radmacher, M., R. W. Tilmann, M. Fritz, and H. E. Gaub. 1992. From molecules to cells: imaging soft samples with the atomic force microscope. *Science.* 257:1900–1905.

Ragsdale, G. K., J. Phelps, and K. Luby-Phelps. 1997. Viscoelastic response of fibroblasts to tension transmitted through adherens junction. *Biophys. J.* 73:2798–2808.

Rotsch, C., K. Jacobson, J. Condeelis, and M. Radmacher. 2001. EGF-stimulated lamellipod extension in adenocarcinoma cells. *Ultramicroscopy.* 86:97–106.

Rotsch, C., K. Jacobson, and M. Radmacher. 1999. Dimensional and mechanical dynamics of active and stable edges in motile fibroblasts investigated by using atomic force microscopy. *Proc. Natl. Acad. Sci. USA.* 96:921–926.

Stossel, T. P. 1993. On the crawling of animal cells. *Science.* 260:1086–1094.

Thoumine, O., and A. Ott. 1997. Timescale-dependent viscoelastic and contractile regimes in fibroblasts probed by microplate manipulation. *J. Cell Sci.* 110:2109–2116.

Tortonese, M., and M. Kirk. 1997. Characterization of application specific probes for SPMs. *Micromach. Imag. SPIE.* 3009:53–60.

Tsai, M. A., R. S. Frank, and R. E. Waugh. 1994. Passive mechanical behavior of human neutrophils: effect of cytochalasin B. *Biophys. J.* 66: 2166–2172.

Tu, Y.-O., and D. C. Gazis. 1964. The contact problem of a plate pressed between two spheres. *J. Appl. Mech.* 31:659–666.

Vorovich, I. I., and I. A. Ustinov. 1959. Pressure of a die on an elastic layer of finite thickness. *PMM.* 23:637–650.

Wachsstock, D. H., W. H. Schwartz, and T. D. Pollard. 1994. Cross-linker dynamics determine the mechanical properties of actin gels. *Biophys. J.* 66:801–809.

Yamada, S., D. Wirtz, and S. C. Kuo. 2000. Mechanics of living cells measured by laser tracking microrheology. *Biophys. J.* 78:1736–1747.

Ziemann, F., J. Rädler, and E. Sackmann. 1994. Local measurements of viscoelastic moduli of entangled actin networks using an oscillating magnetic bead microrheometer. *Biophys. J.* 66:2210–2216.